Combustion and Flame 164 (2016) 303–318

Contents lists available at ScienceDirect

Combustion and Flame

journal homepage: www.elsevier.com/locate/combustflame

Evolution of flame-kernel in laser-induced spark ignited mixtures: A parametric study

Irfan A. Mulla [a,1], Satyanarayanan R. Chakravarthy [b], Nedunchezhian Swaminathan [c], Ramanarayanan Balachandran [a,*]

[a] Department of Mechanical Engineering, University College London, Torrington Place, London WC1E 7JE, UK
[b] Department of Aerospace Engineering, Indian Institute of Technology Madras, Chennai 600036, India
[c] Department of Engineering, Cambridge University, Trumpington Street, Cambridge CB2 1PZ, UK

ARTICLE INFO

Article history:
Received 15 May 2015
Revised 23 November 2015
Accepted 27 November 2015
Available online 22 December 2015

Keywords:
Laser ignition
Flame-kernel
OH PLIF
H-alpha
Laser induced spark

ABSTRACT

The present work focuses on the early stages of flame-kernel development in laser-induced spark ignited mixtures issuing out of a Bunsen burner. The time-scale of 3 μs to 1 ms associated with the flame-kernel evolution stage of an ignition event is targeted in this work. A CH_4/air mixture (equivalence ratio $\phi = 0.6$) is studied as a base case, and compared with CH_4/CO_2/air (mole fractions = 0.059/0.029/0.912, respectively) and CH_4/H_2/air (mole fractions = 0.053/0.016/0.931, respectively) mixtures for nearly the same adiabatic flame temperature of 1649 K. The spatio-temporal flame-kernel evolution is imaged using planar laser induced fluorescence of the OH radical (OH-PLIF), simultaneously with H-alpha emission from the plasma. The H-alpha emission suggests that the plasma time-scale is well below 1 μs. The PLIF images indicate all the stages of kernel development from the elongated kernel to the toroidal formations and the subsequent appearance of a front-lobe. The different time-scales associated with these stages are identified from the rate of change of the kernel perimeter. The plasma is followed by a supersonic kernel-perimeter growth. Larger flame-kernel spread is found in the case of CH_4/H_2 mixtures. A distinct shift in the trends of evolution of LIF intensity and kernel perimeter is observed as the fuel concentration is varied near the lean flammability limit in CH_4/air ($\phi = 0.35$–0.65) and H_2/air ($\phi = 0.05$–0.31) mixtures. The flow velocity (Reynolds number, *Re*) effect in both laminar and turbulent flow regimes (*Re* = ~600–6000) indicates that the shape of the flame-kernel changes at higher velocities, but the size of the kernel does not change significantly for a given time from the moment of ignition. This could be due to a balance between two competing effects, namely, increase in the strain rate that causes local extinction and thus decreases the flame-kernel growth, and increase in the turbulence levels that facilitates increased flame-kernel surface area through wrinkling, which in turn increases the flame-kernel growth.

© 2015 The Authors. Published by Elsevier Inc. on behalf of The Combustion Institute.
This is an open access article under the CC BY license (http://creativecommons.org/licenses/by/4.0/).

1. Introduction

The combustion process is generally triggered by an external source of energy through ignition. Ignition is defined as the transformation of combustible reactants from a nonreactive state to a self-sustained reactive state without further contribution from an ignition source [1]. This definition highlights the significance of the ignition event for reliable operation in practical devices. Over several decades, ignition has been dominated by electric-spark igniters in practical devices such as spark-ignition engines and gas turbines. A comprehensive review of spark-ignition in turbulent non-premixed flames is provided by Mastorakos [2]. Since the advent of lasers in the 1960 s, numerous researchers have exploited them to generate spark. Ever since the early work of Ramsden and Savic [3] on laser-induced spark in air, numerous researchers have investigated this phenomenon.

Laser ignition phenomena are reviewed by Ronney [1], who provided comparison to the classical electric-spark. Laser ignition mechanisms are classified into four categories [1,4]. A *thermal initiation* takes place when the solid target is heated by a laser source, which in turn acts as an ignition source without electrical breakdown. A *resonant breakdown* requires a close wavelength match to photo-dissociate a particular target species that in turn initiates electrical breakdown. A *photo-chemical dissociation* occurs when a target molecule is dissociated at a certain wavelength. A dissociated radical initiates chain reaction, and thus ignition commences without any breakdown. A *non-resonant breakdown* can be realized at any

[1] On research exchange from Indian Institute of Technology Madras, India. Presently at CORIA - UMR 6614, CNRS, INSA de Rouen, 76801 Saint Etienne du Rouvray, France.

* Corresponding author. Fax: +440 2073880180.
E-mail addresses: irfanmulla.ae@gmail.com (I.A. Mulla), r.balachandran@ucl.ac.uk (R. Balachandran).

http://dx.doi.org/10.1016/j.combustflame.2015.11.029
0010-2180/© 2015 The Authors. Published by Elsevier Inc. on behalf of The Combustion Institute. This is an open access article under the CC BY license (http://creativecommons.org/licenses/by/4.0/).

wavelength when the deposited energy density exceeds the breakdown threshold. This process is initiated by seed electrons released from an impurity (dust, aerosol or soot-particles) in the gas upon absorption of photons [5]. The seed electrons accelerate in the induced electric field, which is referred as inverse bremsstrahlung [6]. This in turn generates more electrons from the gas molecules [7], which eventually leads to an avalanche of electrons [1,5]. This non-resonant breakdown mode of ignition has been widely studied, as the wavelength dependence on the breakdown process is not significant [8,9], and thus readily available Nd:YAG lasers can be employed. The pulse energy requirement for non-resonant breakdown is much more than the other three modes of laser ignition [1], yet it is small enough (a few mJ to tens of mJ) for implementing in practical devices. The non-resonant breakdown is also referred to as the laser-induced spark (LIS) ignition. Further details on these four modes of laser ignition can be found in review articles [1,7].

The benefits of laser ignition as compared to the traditional electric-spark ignition have been highlighted by a few authors [1,7,10,11]. The rate and amount of energy deposition can be precisely controlled with laser ignition. Ignition timings can be controlled accurately owing to faster time scales than electric-spark. Additionally, the ignition location can be directed at a favorable region in a combustion chamber. In a fuel-lean mixture, the burn time can be shortened by igniting the mixture at predetermined multiple locations, as demonstrated by [12]. The use of lasers in spark-ignition engines is reported to reduce the frequency of misfiring [13,14]. At higher pressures, as in spark-ignition engines or gas turbine combustors, a spark-plug requires higher voltage potential for reliable ignition [7]. However, the higher voltage could reduce the life of the spark-plug. On the other hand, the energy requirement for LIS reduces with pressure [15]. These advantages motivate researchers to investigate LIS ignition.

Despite these advantages, laser ignition has not yet been used in practical devices such as spark-ignition engines or gas turbines. The major difficulty is the larger size of the laser source relative to the compact spark-plugs. This problem is being progressively solved by use of a compact passively Q-switched Nd:YAG and Cr:YAG lasers, similar to the work of Tsunekane et al. [16]. Although it is reported that the laser ignition could ignite a fuel-lean mixture (within the flammability limit) that cannot be easily ignited with spark-plugs [17,18], the minimum ignition energy required for laser ignition at atmospheric pressure is usually more than that of the electric-spark [19–23]; however, towards lean and rich flammability limits, the differences in the minimum ignition energy are less pronounced [21]. Ignition with the electric-spark is believed to be assisted with the catalytic contribution from the electrodes [8], whereas LIS is free from such electrodes. Additionally, the energy absorbed by the spark in the LIS process is partly lost to the shock-waves [19,24]. The higher energy requirement of LIS is not a major concern [1], as these energy levels (a few tens of mJ) could be achieved with available laser sources.

Thus, laser ignition has potential applications in spark-ignition engines and gas turbines. A continuous or pulsed laser ignition method is proposed to replace the flame-holders in air-breathing propulsion devices. It is argued that the use of a laser source instead of a physical object to hold the flame could avoid the pressure loss across the flame-holders. Such an application has been demonstrated even in a hypersonic scramjet engine [25]. However, this study suggests a pulse energy requirement of 750 mJ at 100 kHz repetition rate to hold the flame continuously. Such significant requirement for supersonic flow could only be met with bulky lasers at the present level of technology, which makes the use of LIS difficult in such applications. In such scenarios, other modes of laser ignition, namely resonant breakdown or photochemical dissociation, may be applied, where the energy requirement is substantially lower than that for non-resonant breakdown.

The physical mechanisms of the ignition event starting from the laser pulse to the propagating flame front has been has been investigated by quite a few researchers [10,19,21,24,26]. The ignition process consists of a sequence of processes, eventually leading to a propagating flame. These processes include plasma formation followed by shock-waves, flame-kernel development, and eventually propagating flames. Each of these processes is identified with their respective time-scales [11,27]. A typical time-scale of flame-kernel development is 1–1000 μs [11,27]. This critical event governs the ultimate fate of the ignition process [24]. The literature related to LIS ignition indicates that information regarding the early stage of ignition and the effect of various key parameters is scarce. Therefore, it is worthwhile to investigate the flame-kernel behavior systematically using advanced laser diagnostics, which in turn could provide further insight and database for model validation.

The LIS ignition studies at atmospheric pressure in unconfined configurations are also reported by numerous researchers [10,21,24,26,28]. The experimental configurations designed for atmospheric pressure are relatively simple. Thus in the present work, we choose the Bunsen burner configuration.

The objective of the present work is to investigate the flame-kernel development of LIS ignited mixtures of various gas compositions under different flow regimes. The flame-kernel is imaged using planar laser induced fluorescence of OH (OH-PLIF). Simultaneously, H-alpha emission from the plasma is also recorded. The flame-kernel in a CH_4/air mixture is spatially and temporally resolved at certain time steps (1–1000 μs) as a base case. The effect of energy of the ignition-laser is investigated. The flame-kernel characteristics near the lean flammability limit (LFL) are investigated in CH_4/air as well as in H_2/air mixtures as a function of fuel concentration. The ignition of the CH_4/air mixture is compared with that of CH_4/CO_2/air and CH_4/H_2/air mixtures for a given adiabatic flame temperature. The choice of composition of these multi-component fuels is motivated by a typical composition of biogas (CH_4/CO_2) and syngas ($CH_4/CO_2/H_2$), which are potential alternative fuels. Additionally, the effect of reactant velocity (and indirectly, turbulence level) on flame-kernel is studied in CH_4/air mixtures.

The fundamental knowledge of the ignition process in a simple experimental configuration acts as a milestone towards our understanding of LIS ignition process in practical high-pressure devices, such as spark-ignition engines and gas turbine combustors. Additionally, the database generated in the present work for a wide variety of conditions can be used to validate numerical simulations of the flame-kernel development.

2. Experimental details and data reduction procedure

2.1. Burner

In most of the past works [8,11,12,19,22,27,29,30], a constant volume combustion vessel has been used, where the mixture is essentially quiescent. In the present work, on the other hand, a Bunsen burner of 10 mm diameter is employed, similar to Beduneau et al. [10,21]. A Bunsen burner operated at atmospheric pressure offers significant simplicity, as there are no optical windows required, which in turn avoids complexity in the experimental set-up. Spiglanin et al. [24] too ignited flowing reactants, but on a McKenna burner. The McKenna burner configuration was also used by Chen and Lewis [26] to visualize laser-induced breakdown and ignition. In the present work, air and fuel are premixed and then issued through the burner at a certain velocity (typically 90 cm/s). For a given combination of equivalence ratio and bulk velocity, the flow rates are predetermined. A number of mass flow meters are used to cover the wide range of gases and flow rates. The air and CH_4 flow rates are metered with thermal flow meters (Vögtlin Instruments) and controlled through high precision needle valves. The flow rates of H_2 and

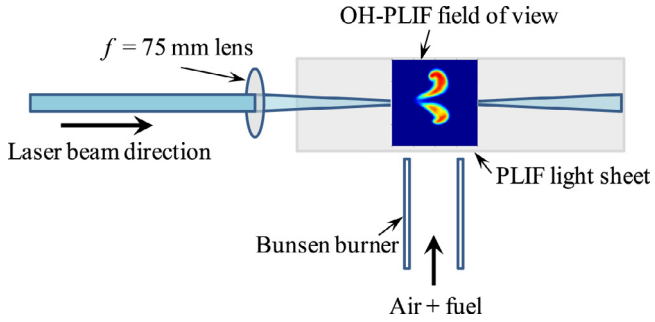

Fig. 1. Schematic of the burner and optical layout.

CO_2 are metered using other thermal flow meters (Bronkhrost High-Tech). Though the mixture is not quiescent, the flow can be assumed quasi-quiescent for the time-scale of interest (1–1000 μs). Such a small bulk velocity is not expected to strongly influence the kernel development, at least during the early stages [21,24]. The velocity of the reactants is intentionally set to achieve flame blow-off conditions. Thus, the mixture is flammable but the flame does not stabilize. This should not be confused with non-igniting flames, where the mixture itself lies outside the flammability limits. The igniting and non-igniting kernels can be distinguished over time-scales of 100–300 μs, as presented in Section 3.5. This experimental configuration and operating conditions enable recording of a large number of samples, treating each ignition event as a time-independent realization. Thus, the experimental efforts are reduced to a great extent, as the data can be acquired continuously without the need for a fresh start/stop cycle of the experiment, with which only one instantaneous image could be obtained per test. This aspect could be appreciated if one compares the number of images obtained in the past work [31], which was 5 with the start/stop cycle, in contrast to 100 realizations that are acquired in the present work. The number of images can be subsequently averaged to improve the fidelity of the data.

2.2. Optical layout

The mixtures are ignited using the third harmonic (355 nm) of an Nd:YAG laser (Litron, LPY 7864-10 model), referred to as the ignition-laser. As discussed earlier in Section 1, the flame-kernel development in the LIS ignition is reported to be nearly independent of the wavelength. The laser beam diameter was reduced to 4 mm using a telescopic arrangement. The laser beam was focused using a quartz plano-convex lens of 75 mm focal length. In the present work, the beam profile is close to Gaussian, thus it is necessary to evaluate the M^2 factor (times diffraction limited). For perfectly Gaussian beam, $M^2 = 1$, however in general $M^2 > 1$. In the present work, the calculated $M^2 = 4.4$. The M^2 value is calculated similar to Bradley et al. [19] using the following parameters: beam diameter (4 mm), beam divergence (0.5 mrad), and wavelength (355 nm). The diameter at the beam-waist is calculated to be 0.04 mm from Gaussian beam theory following [19]. For laser beam profiles with M^2 approaching unity, the diameter at the beam-waist becomes smaller, which consequently facilitates electrical breakdown at lower pulse energies. This is of particular interest for implementation of LIS ignition in practical devices.

Figure 1 shows the schematic of the Bunsen burner and the layout of the ignition-laser beam and the OH-PLIF laser sheet. The beam was focused 13 mm above the burner lip along the axis of the burner. This location ensures that ignition occurs in the potential core of the jet issuing from the burner. Additionally, sufficient space is ensured for development of the flame-kernel at this distance. Kopecek et al. [9] and Weinrotter et al. [11,12] distinguish between MIE and minimum pulse energy (MPE). MIE is the minimum energy required to yield ignition, whereas MPE is the total pulse energy needed for ignition [9,11,12]. Not all of the pulse energy contributes to the formation of the plasma, and hence MPE is always higher than MIE. This is clearly demonstrated [32] by measuring the energy of the incident laser and downstream of the plasma. The MIE or MPE increases with the focal volume (which is commensurate with the focal length of the lens) [9,11,21,33]. Tighter focus can be achieved with an expanded beam and short focal length lens, which is a typical approach used to reduce MIE [19,24,26,27]. Nevertheless, the objective of the present work is not to measure or attempt to reduce MIE, but to study the flame-kernel evolution in general. Here, the mean pulse energy E is typically 138 mJ with a standard deviation of ∼2%. The data is acquired at either 1 or 2 Hz, so that each ignition event is time-independent.

The flame-kernel evolution is imaged using OH-PLIF technique. The PLIF images are acquired at a number of predetermined delays after the ignition-laser pulse (within ± 2 ns). In this manner, the flame-kernel is resolved in both space and time. The OH radical is excited at ∼283 nm. The $Q_1(6)$ line in the $A^2\Sigma^+ - X^2\Pi$ (1, 0) band is excited. A frequency-doubled Nd:YAG laser (Litron, NanoPIV model) is used to pump a tunable dye laser (Fine Adjustments, Pulsare-S model) with the Rhodamine 6 G dye. The fundamental wavelength from the dye laser is frequency-doubled and tuned to generate 283 nm with ∼12 mJ pulse energy. The beam is converted into a light sheet using a plano-concave cylindrical lens and focused by a bi-convex spherical lens. The resulting light sheet is 30 mm in height and ∼0.2 mm in thickness. The PLIF signal is amplified by a UV intensifier and imaged on a CCD camera (TSI, pixel resolution 1376×1024). The camera is equipped with a UV lens and a set of UG11 and WG305 SCHOTT filters to collect the signal around 310 nm within the wavelength range of 309–375 nm. The background flame chemiluminescence is suppressed by gating the camera to 300 ns.

Apart from OH-PLIF, the plasma emission from atomic hydrogen (H-alpha) is also acquired simultaneously. The H-alpha signal is mildly intensified by a visible intensifier and collected on a CCD camera (TSI, pixel resolution 1376×1024). The H-alpha signal from the plasma emission is collected using an interference filter of 655 nm wavelength with a bandwidth of 15 nm. The camera is gated to 60 ns. The delay between the 355 nm (ignition) and 283 nm (OH-PLIF) pulses are controlled independently. Synchronization and timings between the laser pulse, camera exposure, and intensifier gate are controlled through an external electronic synchronizer (Model 610035 LaserPulse Synchronizer TSI). The data is acquired using the Insight® software package (TSI). The ignition-laser beam and the OH-PLIF light sheet are spatially overlapped as illustrated in Fig. 1. The cameras that acquire the H-alpha emission and the OH-PLIF are located perpendicular to and on either side of the PLIF sheet.

2.3. Data reduction procedure

For every experiment, 100 realizations of each OH-PLIF and H-alpha emission are acquired. The images are averaged to reduce the measurement uncertainty. The uncertainty in the mean quantity is estimated as $\pm t_s S_N/\sqrt{N}$, where t_s is the Student's t-factor and S_N is the standard deviation over N realizations. For the confidence interval of 95% and 100 realizations, t_s= 1.984. Consequently, typical uncertainties in the mean LIF and the mean H-alpha signal are ± 0.5% and ± 2% respectively. The averaging also ensures that there are no significant biases introduced due to shot to shot energy fluctuations (typically < 7%, the corresponding standard deviation being 2%). Thus, for each experimental condition, the mean H-alpha image and the mean OH-PLIF image are obtained. A mean background image is subtracted from each respective realization. Further, intensity thresholding based on edge detection is used to discard background noise from the OH-PLIF images. The following four parameters are extracted from the averaged images: 1. peak H-alpha signal, 2. peak OH-PLIF signal, 3. spatially integrated OH-PLIF signal, and 4. flame-kernel perimeter from the OH-PLIF images. The uncertainties in the evaluation of the mean flame-kernel perimeter for the flame-kernels evaluated at 1000 μs and 10 μs time delays are ± 0.4 and ± 1.2%,

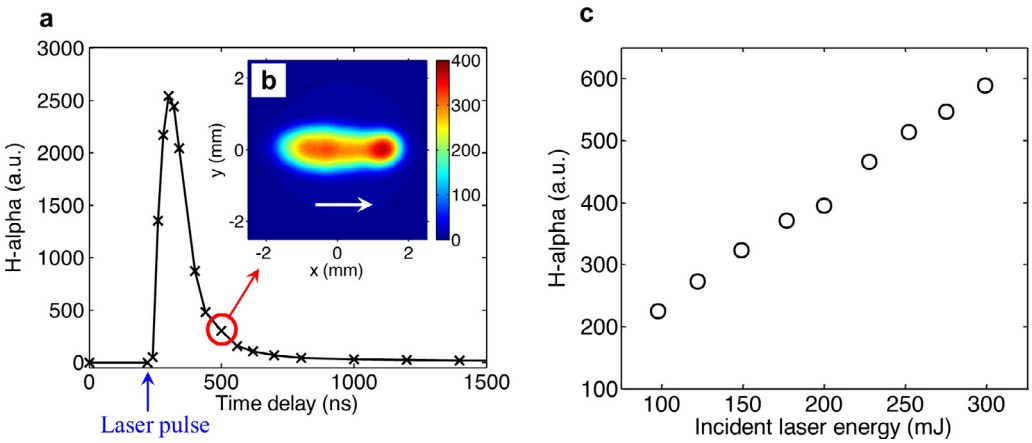

Fig. 2. (a) Temporal variation of H-alpha emission; laser pulse fires ~220 ns. (b) Spatial variation of H-alpha emission at 280 ns after the laser pulse; the white arrow indicates the direction of the laser beam, and the laser focus is approximately at the origin of image co-ordinates. (c) Variation of H-alpha emission with the incident laser energy.

respectively. These uncertainties originate from the limited projected pixel resolution (36 μm).

In the present work, we do not attempt to associate OH-LIF intensity to OH concentration. Nevertheless, we expect the LIF intensity to be in close correlation with OH concentration during the flame-kernel evolution stage (0–1000 μs) of the ignition process. The fluorescence signal is proportional to the fluorescence quantum yield, defined as $A/(A+Q)$, where A is the spontaneous emission (fluorescence) and Q is the collisional quenching rate. In general, $A << Q$, thus the quantum yield can be approximated as A/Q. Note that Q is a function of the local gas composition and temperature. Unfortunately, in the present work, the mixture temperature within flame-kernel is unknown, and hence it is not trivial to incorporate such a correction. However, the past work by Qin et al. [34] provides temperature fields of the flame-kernel over the 3–30 μs time scale in LIS ignited NH_3/O_2 mixtures. These results show the temperature drop from 3000 to 2300 K over a time scale of 3–30 μs. The temperature varies only marginally when ϕ is changed from 0.1 to 1.0. In the present work, though the mixture compositions are different, we expect a similar temperature range due to the weak sensitivity of temperature to the mixture composition during early stages of kernel development. Thus, the temperature is expected to drop from 3000 K to the respective adiabatic flame temperature over the time scale of 10–1000 μs. As shown by Qin et al. [34], the quenching rate does not vary significantly over temperature range of interest (1600–3000 K). Within this temperature range, Q is also shown to be nearly independent of the equivalence ratio (ϕ varied from 0.4 to 1.0). Thus, we may assume the LIF signal to be proportional to the OH concentration over the temperature range of interest. Certainly, these assumptions warrant further work, which is beyond the scope of the present work. One may measure temperature fields and calculate the gas composition assuming chemical equilibrium at a given temperature. From this information, it will be possible to determine the quenching rate, similar to Qin et al. [34].

It should be noted that the averaging does not impact the key observations deduced from the trends in the variation of parameters. This is demonstrated subsequently in Sections 3.2 and 3.6 for the laminar and turbulent flow cases respectively. Further, past work [26] suggests that the characteristics of the flame-kernel are highly repeatable, despite the stochastic nature of the breakdown process. This observation holds true to certain extent even in a turbulent flow field [25]. This is not very surprising if one compares the time-scales of the laser-induced flame-kernel development (1–1000 μs) with that of the flow time-scales (1–2 orders of magnitude higher).

The location of the beam focus (observed from the H-alpha images) showed a mild variation (0.1–0.15 mm) from shot-to-shot. This is attributed to the well-known shot-to-shot variation of the laser beam pointing stability. Two approaches of data processing could be adopted to address this, as done in the present work. In the first approach, the peak values can be extracted from each instant and then averaged. In the second approach, the images can be averaged and then the average image can be used to extract the values. The results obtained using the later method should be treated with caution for the turbulent flow cases. However, in the present work, the observed trends and the conclusions arrived at are insensitive to both the approaches of data processing (see Section 3.6).

3. Results and discussion

3.1. Characterization of laser-induced spark in pure air

The laser-induced spark is characterized in pure air before performing experiments with fuel/air mixtures for ignition. Figure 2 shows the mean H-alpha emission from the plasma, which is acquired at ~280 ns after the laser pulse. The mean pulse energy of the laser is measured to be 145 mJ. The shot-to-shot energy fluctuations are within 7% and the corresponding standard deviation is 3 mJ. Note that, in spite of the precise timing synchronization, the laser pulse could not be located to sub-nanosecond accuracy. In the present work, the rising edge of the H-alpha emission is assumed to be the start of the ignition event. The arrow in Fig. 2(b) indicates the direction of the laser beam. This image appears similar to the plasma emission reported in [10]. Figure 2(a) shows the H-alpha evolution, which is resolved to 20 ns. The peak value (spatially) of the H-alpha emission is extracted from the averaged images obtained at different time delays. Following the ignition-laser pulse, the H-alpha emission rises sharply and drops asymptotically. The trend of this variation is in agreement with the temporal profile of the plasma emission [33]. This temporal profile confirms the time-scale of the plasma emission (~1–1000 ns) illustrated by Weinrotter et al. [11,12].

Next, the effect of laser energy on the H-alpha signal is investigated. The laser energy is varies from 100 mJ to 300 mJ. Within this range, the variation in the H-alpha signal is found to be linear, as shown in Fig. 2(c). This linear relationship could be exploited to correct for any energy drift of the laser without the need for online energy measurement, provided that the gas composition and the flow velocity remain constant. This aspect is utilized in the present work wherever appropriate.

In addition, the extent of energy utilization by the spark is characterized. The laser energy is measured upstream and downstream of the plasma, similar to [32]. At a mean incident laser energy of 122 mJ, only ~29 % of the energy is utilized in the formation of the plasma measured in pure air. This value is significantly different from the one calculated from the linear relationship (~72%) provided by Morsy et al. [32]. The reason for this discrepancy is not

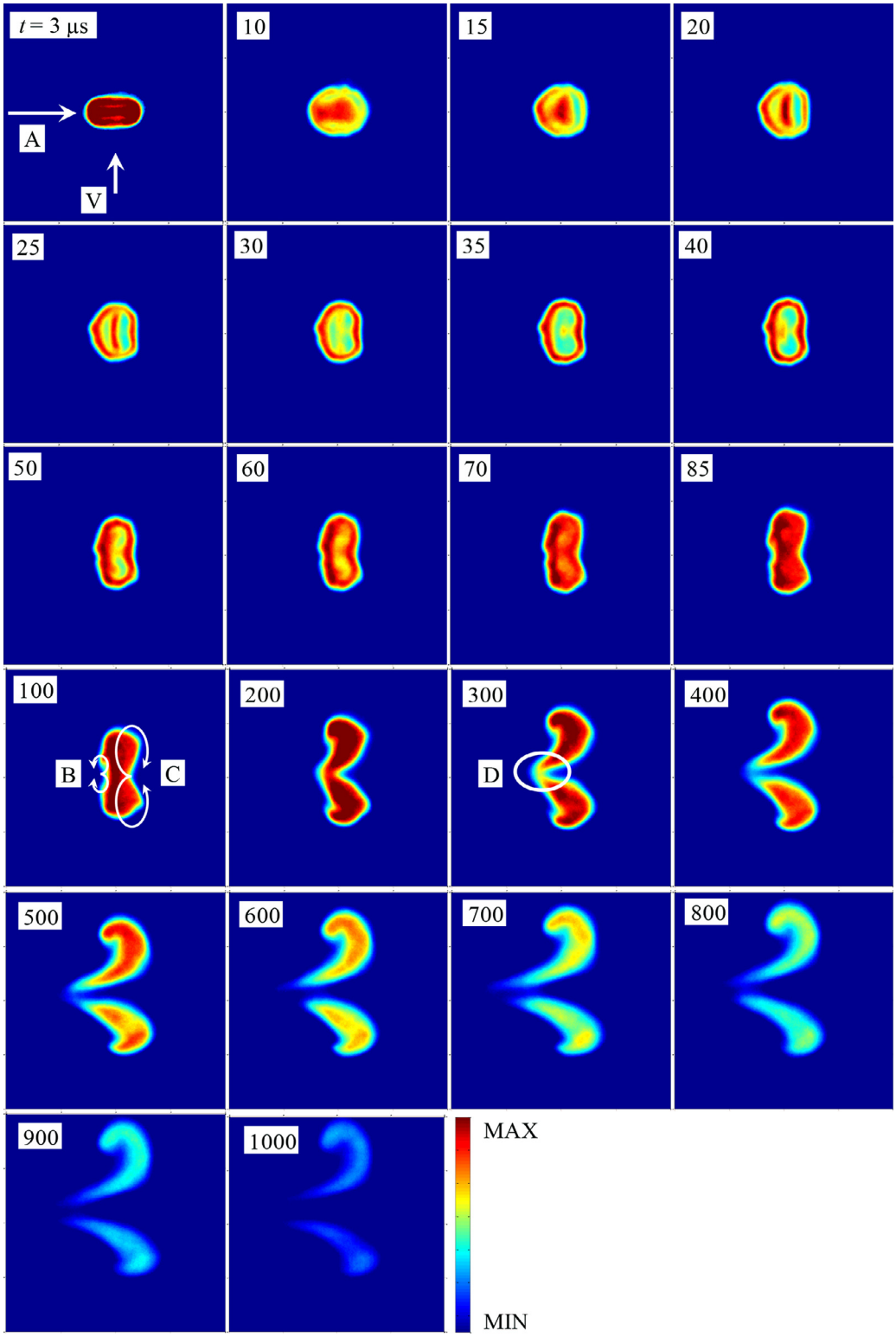

Fig. 3. Evolution of mean OH-PLIF images in the $\phi = 0.6$ CH_4/air mixture. The numbers in the insets are time delays in μs after the incident laser pulse. Images are 20 mm × 20 mm in size. All the images are plotted on the same contour scale. A: direction of the ignition-laser, B: small and weak toroid, C: large and strong toroid, D: front-lobe, V: direction of the flow (as depicted in Fig. 1). The mean pulse energy of the ignition-laser $E = 138$ mJ.

investigated in the present work. However, it is important to note that, in the present work, the energy measured significantly varies with the downstream distance from the epicenter of plasma. This suggests the diffraction or wider divergence of the laser beam downstream of the plasma; however, this could only be substantiated with further investigation.

3.2. Flame-kernel evolution in CH_4/air

A CH_4/air mixture at an equivalence ratio $\phi = 0.6$ and bulk velocity $V = 90$ cm/s is issued through the burner. In this mixture, the flame-kernel evolution is recorded using OH-PLIF images. Figure 3 shows the sequence of the mean OH-PLIF images acquired at various time

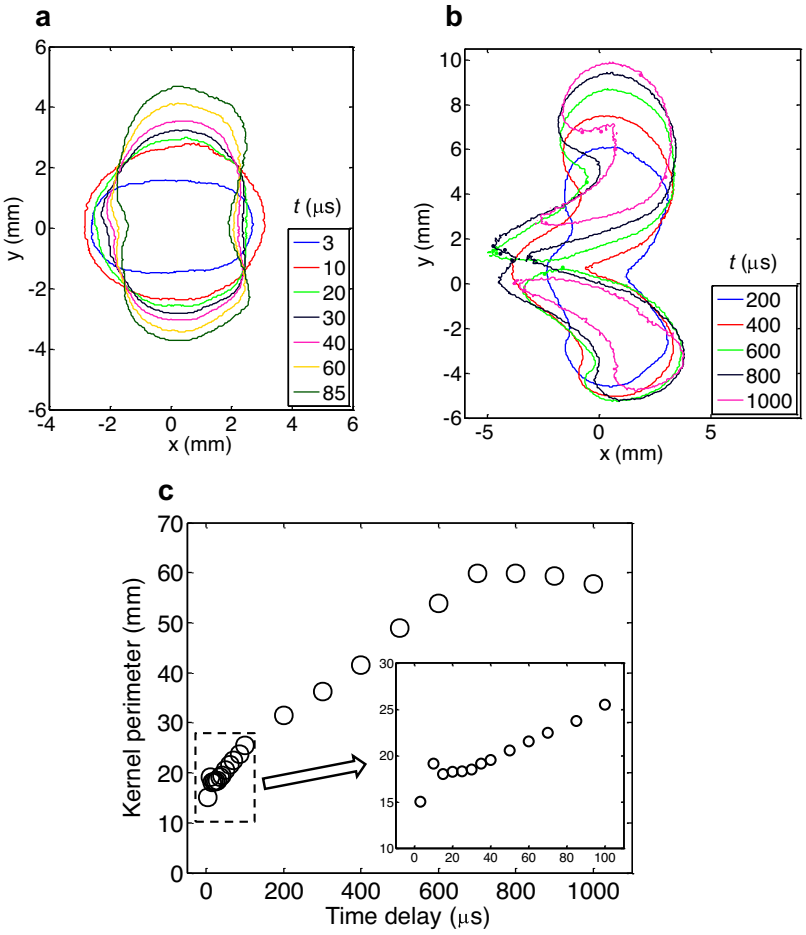

Fig. 4. Flame-kernel evolution of the $\phi = 0.6$ CH_4/air mixture: (a) flame-kernel from 3 to 85 μs, (b) flame-kernel from 200 to 1000 μs, and (c) flame-kernel perimeter versus time.

delays with respect to the ignition-laser pulse. The mean energy of the incident ignition-laser pulse was measured at 138 mJ with < 7% shot-to-shot fluctuations in these experiments. Imaging is performed at 22 different time delays to adequately resolve the flame-kernel evolution temporally. The flame-kernels are resolved spatially in 2D with a projected pixel resolution of 36 μm/pixel.

The shapes of the evolving flame-kernel are in close agreement with those reported in past works [10,21,24,26,27,29]. A detailed discussion on the physical mechanism of the flame-kernel evolution is provided by Spiglanin et al. [24] and Bradley et al. [19]. At 3 μs, a strong PLIF signal is observed and the flame-kernel appears elongated rather than spherical. The plasma does not uniformly absorb the energy from the laser along the beam. The rate of energy absorption exponentially decays along the laser beam [19]. With respect to the incident laser (or focusing lens), the epicenter of the shock-wave is reported to lie ahead of the centroid of the plasma [19,24]. Two contra-rotating toroids are generated through a complex process of interaction of the shock-wave and the rarefaction-wave with the hot plasma, as explained by Kono et al. [35] through simulations. Upstream of the plasma, small and weak toroids (indicated by *B* in Fig. 3) are generated, whereas downstream of the plasma, large and strong toroids (indicated by *C* in Fig. 3) are produced. This inequality is explained through the offset of the epicenter of the shock-wave and the centroid of the plasma in [19]. The non-uniform rate of energy absorption by the plasma along the laser beam also contributes to this asymmetry. The inception of these contra-rotating toroids occurs at ~30 μs. The large toroid continues to prevail, while the small toroid decays after 100 μs.

The propagation of the flame-kernel along the laser beam (indicated by *D* in Fig. 3) is unique to laser-ignition, which precipitates around 200 μs. This extension of the flame-kernel is also known as the front-lobe [27,29,36] or the third lobe [19]. Multiple contributing factors toward the generation of this lobe are explained by Spiglanin et al. [24] and Bradley et al. [19]. These factors are briefly listed here:

(1) Preheating of the gases upstream of the plasma by a weakly focused laser beam enhances the flame-kernel propagation along the laser beam [24].
(2) The plasma itself is reported to propagate towards the laser source [24,37]. The flame-kernel subsequently follows the plasma. However, it is argued that this propagation would cease shortly after the laser pulse [19].
(3) Offset of the intense region of spark with respect to the center of the spark volume [24], as stated earlier.
(4) Asymmetry in the upstream and downstream toroids that generates a centerline velocity towards the laser source [19].

Next, the flame-kernel shapes are extracted from the PLIF images following the gradient in the contours. The flame-kernels at different times are overlaid for comparison, as shown in Fig. 4. The flame-kernels are plotted only for 12 time steps in this figure for the sake of brevity and clarity. A mild effect of the bulk flow velocity on the flame-kernel evolution is observed at longer time-scales (600–1000 μs) in Fig. 4(b). The flame-kernel perimeter is extracted from these flame-kernel shapes, and plotted in Fig. 4(c). The kernel perimeter is shown separately in the inset for the 3–100 μs time interval, for clarity. The distinct time-scales can be observed from the

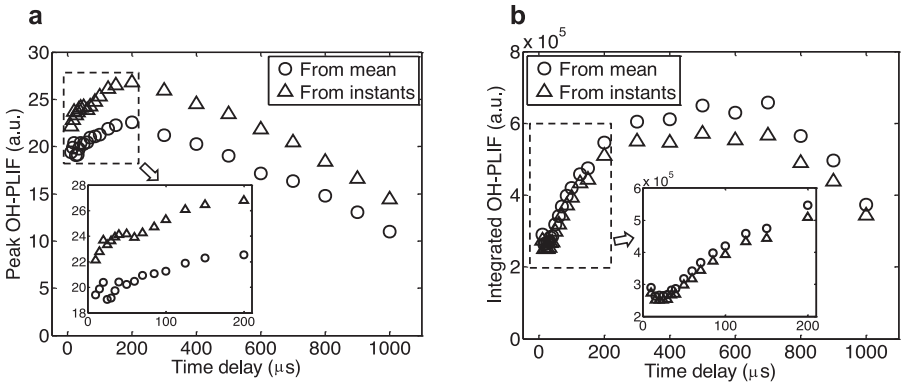

Fig. 5. Variation of OH-PLIF intensities with time for the $\phi = 0.6$ CH_4/air mixture: (a) peak PLIF intensity, and (b) spatially-integrated PLIF intensity. Data is extracted directly from the mean PLIF image (circles); alternatively, data is extracted from instantaneous images and then averaged (triangles).

slopes. For the first 10 μs, a sharp increase in the kernel perimeter is observed. From 10 to ~35 μs, a plateau is observed, followed by a constant rate of increase in the kernel perimeter till 100 μs. The rate of increase in the perimeter reduces mildly during 200–700 μs, followed by saturation till 1000 μs.

The mean PLIF images are also used to extract the peak OH-PLIF signal (Fig. 5(a)) and spatially integrated PLIF signal (Fig. 5(b)). The data processing is performed following both the approaches mentioned earlier: values are extracted directly from the mean PLIF images (circle marks) in the first approach, whereas data is extracted from the instantaneous images and then averaged (triangle marks). It can be observed from Fig. 5 that the values are different as expected, but the trends in the variation are identical. Thus, any processing method out of the above two is found to be suitable in the present work. In subsequent sections, therefore, the data extracted directly from the mean images are presented.

In Fig. 5, the data for 0–200 μs is shown separately in the inset for clarity. The LIF values corresponding to 3 μs are not plotted. The LIF intensity at 3 μs is expected to be affected by residual plasma emission, which may override the LIF signal. Such observation has been noted by Qin et al. [34]. Thus, the LIF data at 3 μs is used only to evaluate the flame-kernel perimeter, which is deduced through the gradient in the LIF signal, and hence not affected significantly by the residual plasma emission.

The variation of the peak LIF signal with time is quite systematic and almost free of scatter. The LIF signal increases for the first 200 μs, reaches a peak, and falls at a constant rate till 1000 μs. This behavior may be explained through the competition of OH production, consumption and quenching. The quenching rate of the LIF signal decreases asymptotically with temperature. At higher temperature (>1600 K), the variation in the quenching rate is expected to be less pronounced [34]. During the early stages (0–200 μs), the high temperature (~2500–3000 K) may enhance the production of OH. Over the next few milliseconds, the mixture temperature is expected to drop to the adiabatic flame temperature (~1650 K) from a high value (~2500 K). Thus, the variation in the quenching rate can be slightly more pronounced than during 0–200 μs. Additionally, the net consumption of OH at such a low temperature explains the monotonic drop in LIF signal from $t > 200$ μs. Therefore, the peak in the LIF signal can be explained as the balance between OH production at high temperature, consumption at moderate temperature, and a mild variation of the quenching rate due to change in the temperature. These competing effects cause an optimum, which results in a peak in the OH LIF signal at t ~200 μs.

Next, the LIF intensity values are spatially integrated to indicate the *strength* of the flame-kernel. Similar to the peak LIF intensity, the integrated signal increases till 200 μs, but reaches a plateau thereafter till 700 μs, and then decreases at a constant rate till 1000 μs.

3.3. Effect of ignition-laser energy

In this section, the effect of the incident laser energy is reported. The pulse energy of the incident ignition-laser is varied from 98 mJ to 268 mJ, and the PLIF signals for the CH_4/air mixture with $\phi = 0.6$ are imaged.

Figure 6(a) shows the mean PLIF images acquired at 40 μs after the ignition-laser pulse. The peak LIF signal is fairly insensitive to the change in the ignition-laser energy. Over this range (98–268 mJ) of laser energy, the peak OH-LIF signal changes only by ~4%. On the other hand, the spatially integrated LIF signal shows a strong dependence of the ignition-laser energy, as shown in Fig. 6(b). The wider flame-spread can also be observed directly from Fig. 6(a). The shock-wave intensity increases with the laser energy, and the larger flame-spread is associated with stronger shock-waves. The variation of the integrated LIF is nearly linear with the pulse energy of the incident (ignition-laser) beam. Again, the data is extracted directly from the mean PLIF image (circle marks) and alternatively, from the instantaneous images and then averaged (triangle marks). The differences in the trends and the values are not significant, as observed from Fig. 6(b). Following this demonstration, only data extracted directly from the mean PLIF images is presented in the subsequent subsections.

Additional experiments are performed to investigate the effect of the ignition-laser energy at other time delays as well for the $\phi = 0.6$ CH_4/air mixture. Figure 7(a) shows the peak OH-LIF signal at different energies. The trend in the variation is similar to that shown in Fig. 5(a). The LIF values in Fig. 5 corresponding to 3 μs are not plotted, due to possible interference from the plasma emission.

The peak LIF signal is not significantly sensitive to the laser pulse energy, yet the values still systematically depend on the respective energies. The intensity of the LIF signal correlates well with the pulse energy of the ignition-laser. On the other hand, the spatially integrated PLIF intensities (see Fig. 7(b)) vary strongly with the energy. The sensitivity of the integrated signal appears to be the highest around 300 μs, and the differences tend to get minimized thereafter, as noted at 1000 μs in Fig. 7(b). The dependence of the integrated PLIF on the energy can be better understood from Fig. 7(c), where the integrated PLIF values are normalized with the respective laser energies. The normalized spatially-integrated LIF signals for the different energies tend to collapse over each other, especially for 128 mJ and 187 mJ.

The flame-kernel perimeter is extracted from the mean PLIF images and plotted in Fig. 8 for the different ignition-laser energies. The kernel perimeter increases with the laser energy, as observed from Fig. 8(a). From the moment of the spark, the perimeter continues to grow till 600 μs, and then depending on laser energy, either reduces (88 mJ), saturates (128 and 187 mJ), or continues to rise (226 mJ). In Fig. 8(b), the perimeter P is normalized with the

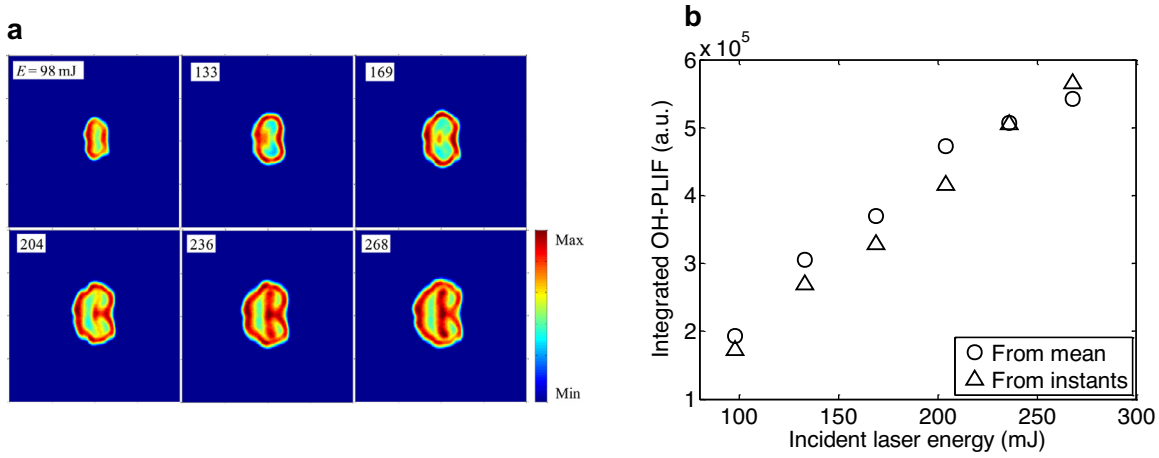

Fig. 6. (a) Mean OH-PLIF images in a $\phi = 0.6$ CH_4/air mixture at different energies after 40 μs from the ignition-laser pulse. The numbers in the inset are the pulse energies of the incident ignition-laser in mJ. Images are 20 mm × 20 mm in size. All the images are plotted on the same contour scale. (b) Variation of the spatially-integrated PLIF intensity with the incident ignition-laser energy.

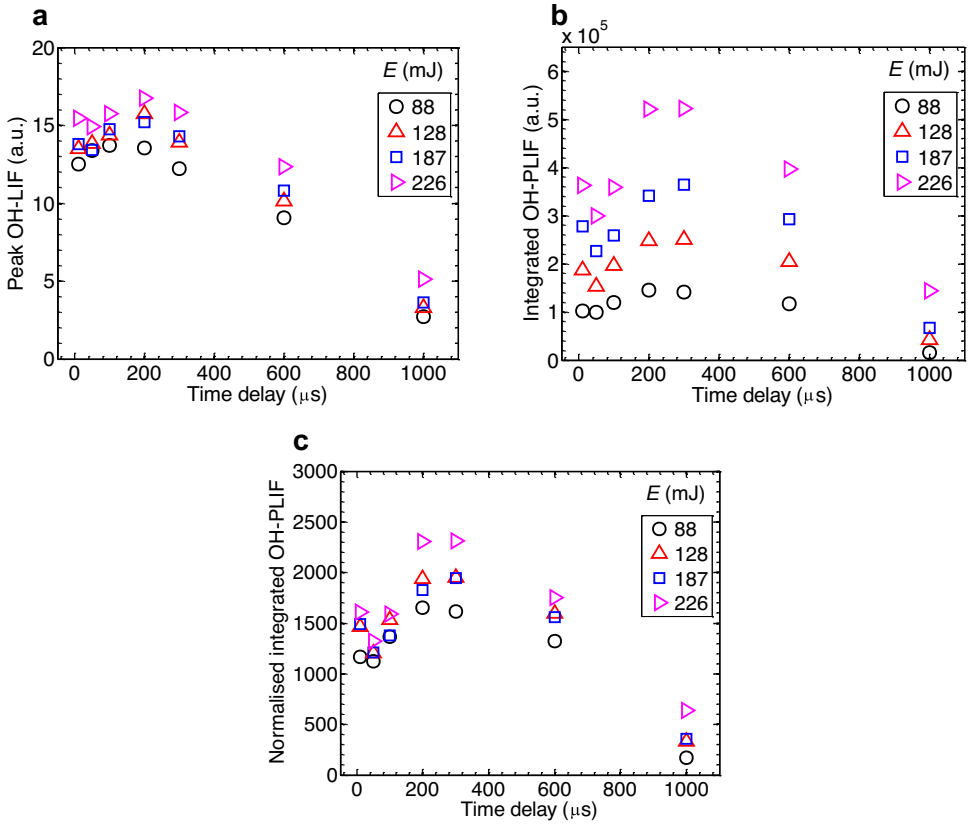

Fig. 7. Variation of OH-PLIF intensities with time of a $\phi = 0.6$ CH_4/air mixture at different energies: (a) peak LIF intensity, (b) spatially-integrated PLIF intensity, and (c) normalized integrated PLIF signal. The numbers in the legends are pulse energies of the incident ignition-laser E in mJ.

corresponding perimeter at $t = 3$ μs (P_0). The normalization performed in this manner tends to reduce the effect of the ignition-laser energy, as observed from the trends in Fig 8(b). The normalized perimeter nearly collapses up to 600 μs, and subsequently, the effect of the laser energy becomes apparent. The perimeter P/P_0 at 50 μs measures the maximum for the lowest laser energy. This behavior could be explained with the evolution of the growth in the flame-kernel perimeter, which is plotted in Fig. 8(c). The growth rate around 7 μs appears to be supersonic, which confirms the existence of shock-waves. Overall, the perimeter growth appears to be the highest for the largest laser energy, except around 30–50 μs, at which the kernel growth is the highest for the lowest energy similar to that in Fig. 8(b). At higher energy (128–226 mJ), the kernel perimeter locally peaks around 75 μs, but not for the 88 mJ. This could be due to the fact that at a higher energy, a stronger shock associated with the first peak at 7 μs leads to a stronger expansion-wave (associated with negative peak at 30 μs), followed by a weaker pressure wave (associated with the second peak at 75 μs), and so on. At lower energy, these effects are less pronounced. This suggests that a higher laser energy cannot always ensure a more efficient flame-kernel growth.

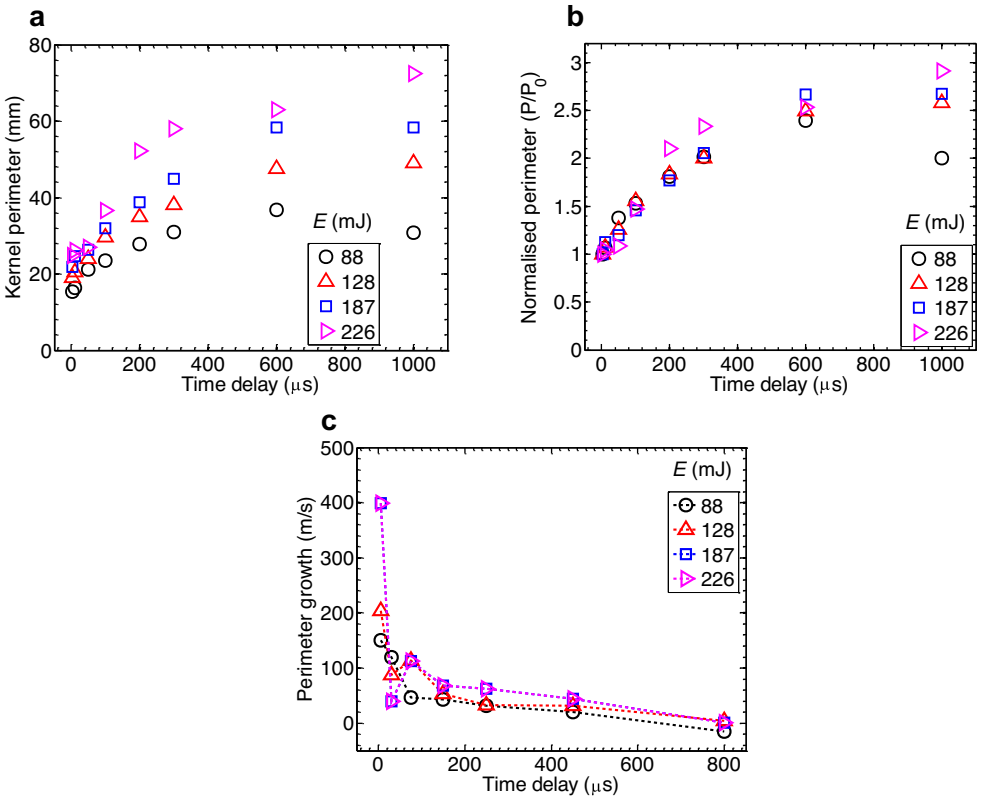

Fig. 8. Variation of the flame-kernel perimeter of a $\phi = 0.6$ CH_4/air mixture at different energies: (a) non-normalized, (b) normalized with respective to the perimeter at $t = 3$ μs, and (c) evolution of the perimeter growth. The numbers in the legends are pulse energies of the incident ignition-laser E in mJ.

3.4. Effect of gas composition for a given adiabatic flame temperature

In Section 3.2, detailed results were presented with a fine temporal resolution (22 time delays). For further experiments, only 7 time delays are selected, however. This reduces the experimental and data processing efforts without significantly altering the interpretation of results. The effect of gas composition is reported in this section. The CH_4/air mixture ($\phi = 0.6$, $V = 90$ cm/s) is taken as the base case, and this is compared with the CH_4/CO_2/air and CH_4/H_2/air mixtures, at the same mixture velocity of $V = 90$ cm/s. The experiments are performed under identical conditions (ignition-laser energy, LIF excitation wavelength, etc.) except the variation in the mixture compositions. For a meaningful comparison, the mixture composition is calculated to have nearly the same adiabatic flame temperature. The gas compositions are listed in Table 1. The adiabatic flame temperature and the flame speed are calculated using the PREMIX code of the CHEMKIN package [38]. The atomic fractions of the compositions are also listed in Table 1.

Similar to the earlier sections, the response of the OH-PLIF signal with time is plotted in Fig. 9 for all the three gas compositions considered. The mean ignition-laser pulse energy is measured at 126 mJ. The PLIF images are acquired at the following eight time delays: 3, 10, 30, 60, 100, 300, 500, and 1000 μs. As explained earlier in Section 3.2, the PLIF data at 3 μs is used only for evaluating the flame-kernel perimeter. The peak LIF signal plotted in Fig. 9(a) is observed to be weakly dependent on the composition. Overall, the peak LIF signal correlates well with the respective atomic fraction of H-atom and O-atom (see Table 1) across the gas compositions. The trends in the variation of the LIF signal for all the gases are similar to that in Fig. 5(a). The LIF signal in Fig. 9(a) peaks between 100 and 300 μs, probably at 200 μs, as observed earlier in Fig. 5(a). Further, the spatially-integrated PLIF intensity is plotted in Fig 9(b). The trend is slightly different from that of Fig. 5(b), as the ignition-laser energy is not identical. Similar to the peak LIF signal, the integrated LIF signal too correlates well with the respective atomic fractions of H-atom and O-atom. The integrated signal appears to peak at 300 μs for the CH_4 and CH_4/CO_2 cases. The trends for CH_4 and CH_4/CO_2 are nearly identical; however, the values for CH_4/CO_2 are slightly higher than that of the CH_4 case. On the other hand, the integrated signal is significantly higher for the CH_4/H_2 case than the rest, indicating a stronger LIF signal and wider flame-kernel spread. The integrated signal appears to peak at 600 μs, unlike the other two mixtures.

The flame-kernel perimeters for all the three cases are plotted in Fig. 9(c). The variation of the perimeter is similar to that in Fig. 5(c) for the CH_4 case. The perimeter for the CH_4/H_2 case measures significantly higher than the CH_4 case throughout the present range of time-scales. The CH_4/H_2 case does not show a plateau between 600–1000 μs, unlike the CH_4 and CH_4/CO_2 cases. The flame-spread enhances with the addition of H_2 for a given adiabatic flame temperature. The trend in the variation of the CH_4/CO_2 case is very different. For the first 100 μs, the perimeter measures significantly higher than the CH_4 case, and lies close to the CH_4/H_2 case. Beyond 100 μs, there appears to be a shift in the trend: during 300–1000 μs, the perimeter values are close to that of the CH_4 case and mildly higher than that of the CH_4 case. This result suggests that, at an adiabatic flame temperature of ~1649 K, during the first 100 μs, the trend in the perimeter variation is independent of the gas composition. However, the effect of the gas composition is apparent after 300 μs. This observation is in very good agreement with the conclusion of the previous work on H_2/air mixtures [24].

Additionally, the peak H-alpha values are extracted from the mean H-alpha emission images at 280 ns after the ignition-laser pulse for the different compositions (similar to one shown in Fig. 2(b)). The H-alpha emission in arbitrary units measures 588, 612, and 647 for the CH_4/air, CH_4/CO_2/air, and CH_4/H_2/air mixtures respectively. These values are commensurate with the H-atom fractions listed in Table 1

Table 1
Gas compositions considered in the present study.

Case	Mole fraction					Atomic fraction				T_{adb} (K)	S_L (cm/s)
	O_2	N_2	CH_4	H_2	CO_2	O	N	C	H		
CH_4	0.198	0.744	0.058	0.000	0.000	0.198	0.744	0.012	0.047	1649.1	10.6
CH_4/CO_2	0.192	0.720	0.059	0.000	0.029	0.211	0.720	0.021	0.048	1649.0	9.9
CH_4/H_2	0.195	0.735	0.053	0.016	0.000	0.195	0.735	0.011	0.059	1647.1	12.3

T_{adb}: adiabatic flame temperature; S_L: laminar flame speed.

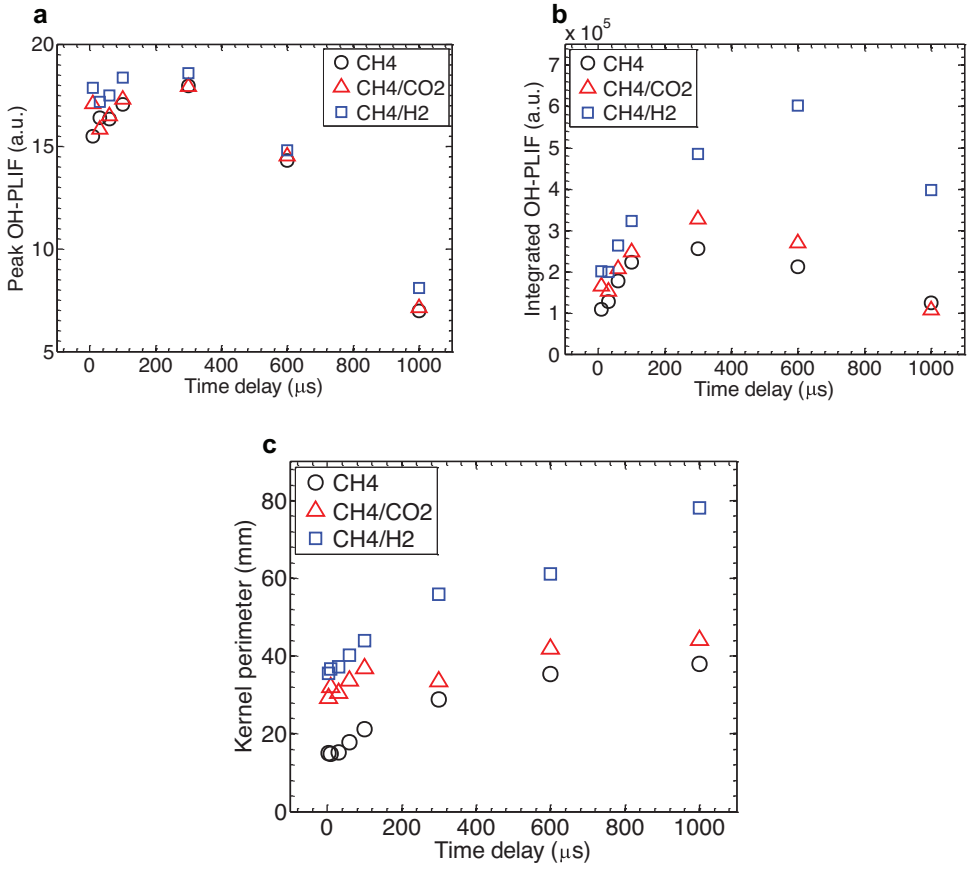

Fig. 9. Evolution of the flame-kernel for different gas compositions: (a) peak PLIF intensity, (b) spatially-integrated PLIF intensity, and (c) flame-kernel perimeter. The pulse energy of the ignition-laser $E = 126$ mJ.

3.5. *Effect of fuel concentration near the lean flammability limit (LFL)*

A mixture can be successfully ignited only if the fuel concentration lies within the flammability limits. To explore the ignition behavior at the edge of the LFL ($\phi = 0.49$ for methane and $\phi = 0.12$ for hydrogen [39]), ignition experiments are performed with varying fuel concentrations near the LFL. CH_4/air and H_2/air mixtures are used for these experiments. Table 2 lists the fuel concentrations both in terms of percentage of air by volume and equivalence ratio. The flow rates are calculated to have a bulk velocity of 90 cm/s for CH_4/air and 130 cm/s for H_2/air. The mean PLIF images for CH_4/air mixtures are not shown here, as such images are already presented in Fig. 3 for one of the equivalence ratios. Instead, information extracted from the mean PLIF images is presented here.

Figure 10 shows the effect of equivalence ratio (or fuel concentration) for CH_4/air mixtures. The PLIF images are acquired at the following eight time delays: 3, 10, 50, 100, 200, 300, 600, and 1000 μs. Again, the PLIF data at 3 μs is used only for evaluating the flame-kernel perimeter. The peak LIF intensity (Fig. 10(a)) shows a mild increase with the fuel concentration. During 10–100 μs, the LIF intensity is less sensitive to the fuel concentration. Beyond 100 μs, the LIF signal drops significantly for $\phi = 0.35$ relative to the other equivalence ratios considered. By 1000 μs, the LIF intensity drops to zero for $\phi = 0.35$ and 0.45, which are below the LFL. The spatially integrated PLIF signal (Fig. 10(b)) increases with the fuel concentration, similar to the LIF intensity shown in Fig. 10(a). The integrated PLIF

Table 2
Gas compositions for variation of fuel concentration.

S. no.	Fuel type	Fuel flow (% by volume)	Equivalence ratio ϕ
1	CH_4	3.64	0.35
2	CH_4	4.64	0.45
3	CH_4	5.68	0.55
4	CH_4	6.72	0.65
5	H_2	2.00	0.05
6	H_2	4.00	0.10
7	H_2	6.00	0.14
8	H_2	10.00	0.24
9	H_2	13.00	0.31

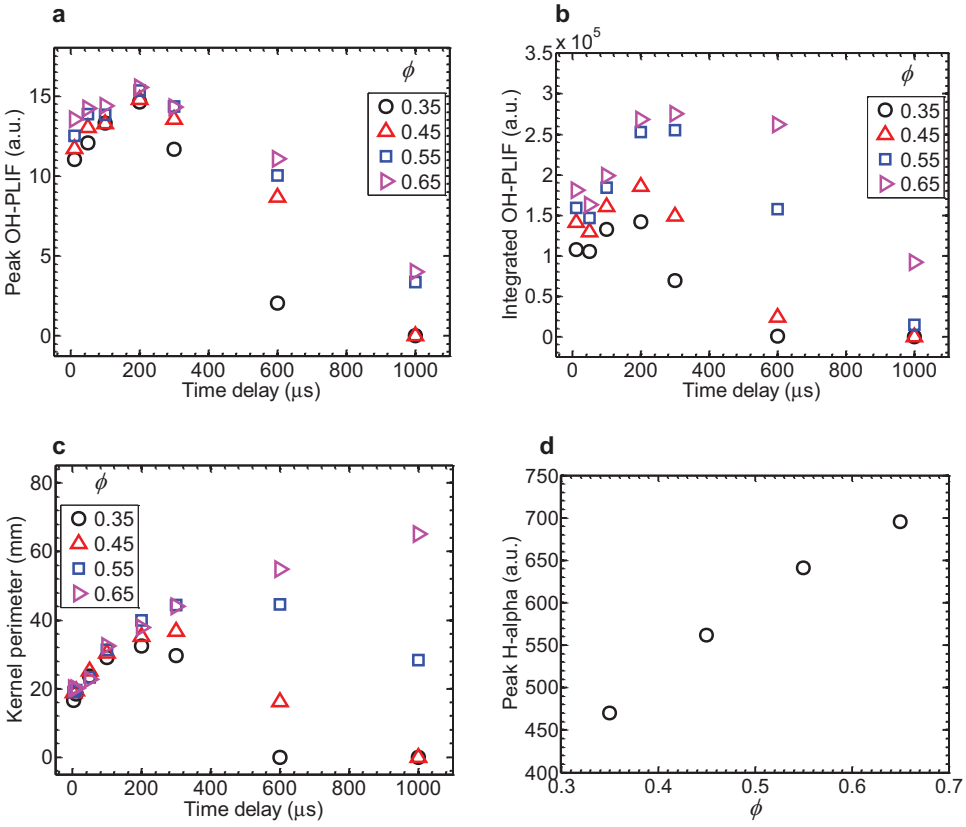

Fig. 10. Effect of equivalence ratio for CH_4/air mixture (equivalence ratios are indicated in legends): (a) peak PLIF intensity, (b) spatially-integrated PLIF intensity, (c) flame-kernel perimeter, and (d) H-alpha emission intensity at 280 ns after the laser pulse. The mean pulse energy of the ignition-laser $E = 128$ mJ.

signal in Fig. 10(b) shows a rise for the first 200 μs irrespective of the fuel concentration. From 200 μs, the signal drops for $\phi = 0.35$ and 0.45, while it stays nearly constant till 300 μs for $\phi = 0.55$ and subsequently drops at a constant rate till 1000 μs. A similar transition does occur for $\phi = 0.65$, which is well above the LFL, but at 600 μs.

Next, the kernel perimeter is presented in Fig. 10(c). The kernel perimeter is nearly independent of the fuel concentration till 100 μs. From 200 μs, it starts to differ progressively with the time delay, depending on the fuel concentration. For $\phi = 0.35$, the perimeter peaks at 200 μs and drops thereafter, whereas for $\phi = 0.45$, it peaks at 300 μs and drops subsequently, and for $\phi = 0.55$, which is just above LFL, such transition occurs at 600 μs. For a mixture well within the flammability limit ($\phi = 0.65$), the kernel perimeter continues to increase till 1000 μs, albeit at a slower growth rate with time. These results identify the important time-scale of 200–300 μs, when the behavior of mixtures within the flammability limit and those outside the limit becomes distinct. This result suggests that the early flame-kernel development is plasma-assisted, which was referred as an *overdrive* by Bradely et al. [19]. The peak LIF signal (Fig. 10(a)) rises sharply for lower equivalence ratios. This result supports the observation noted by Bradley et al. [19] that the leaner mixtures are overdriven strongly than the stoichiometric (or relatively richer) one. The H-alpha emissions are plotted in Fig. 10(d). The H-alpha intensity varies almost linearly with CH_4 concentration (or ϕ) for the present range of equivalence ratio.

Further experiments are performed to assess the applicability of the conclusions drawn from the above results of a hydrocarbon fuel to hydrogen fuel. Based on the results in Fig. 10, the data at only five following time delays are acquired: 10, 30, 100, 300, and 500 μs. No significant information is lost (as compared to Fig. 10) due to these limited data points. In fact, the observations are very similar as of the CH_4/air presented in Fig. 10. The mean PLIF images of the H_2/air mixture are presented in Fig. 11. The PLIF images are shown for the five time delays and for five different equivalence ratios listed in Table 2. The overall flame-kernel shapes and sizes are identical for the first 100 μs, irrespective of the H_2 concentration. The effect of H_2 concentration appears from 300 μs onwards. At 500 μs, the LIF signal disappears for $\phi = 0.05$, whereas only a weak LIF signal is observed for $\phi = 0.10$.

The peak LIF intensity plotted in Fig. 12(a) is nearly independent of the fuel concentration for the first 100 μs. The LIF intensity drops after 100 μs at different rates depending on the fuel concentration: at lower ϕ, the LIF intensity drops at a higher rate. It disappears by 500 μs for $\phi = 0.05$, which is well below the LFL. The variation of the spatially-integrated PLIF signals for different equivalence ratios are presented in Fig. 12(b). The integrated signal increases during the first 100 μs. Afterwards, the signal begin to drop for $\phi = 0.05$ and 0.10, which are below the LFL. For $\phi = 0.14$ (just above the LFL), the integrated signal peaks at 300 μs and drops subsequently. On the other hand, for $\phi = 0.24$ and 0.31 (well above the LFL), the signal does not show any drop, though the rate of increase slows down significantly during 300–500 μs.

The flame-kernel perimeter is plotted in Fig. 12(c). The perimeter increases nearly at the same rate during the first 300 μs irrespective of the H_2 concentration. After 300 μs, the kernel perimeter drops for $\phi = 0.05$ and 0.10 mixtures, while it continues to grow (till 500 μs) for mixtures with higher equivalence ratios. The rate of growth of the perimeter is nearly identical for mixtures above the LFL. The kernel perimeter measures nearly identical for mixtures above the LFL ($\phi = 0.14$–0.31). Similar to the CH_4/air mixtures, the time-scale of 100–300 μs appears to be relevant to the H_2/air mixtures as well, during which the changes in the flame-kernel perimeter become distinct depending on whether the mixture is above or below the LFL. The H-alpha intensity in the case of the H_2/air mixtures also varies linearly

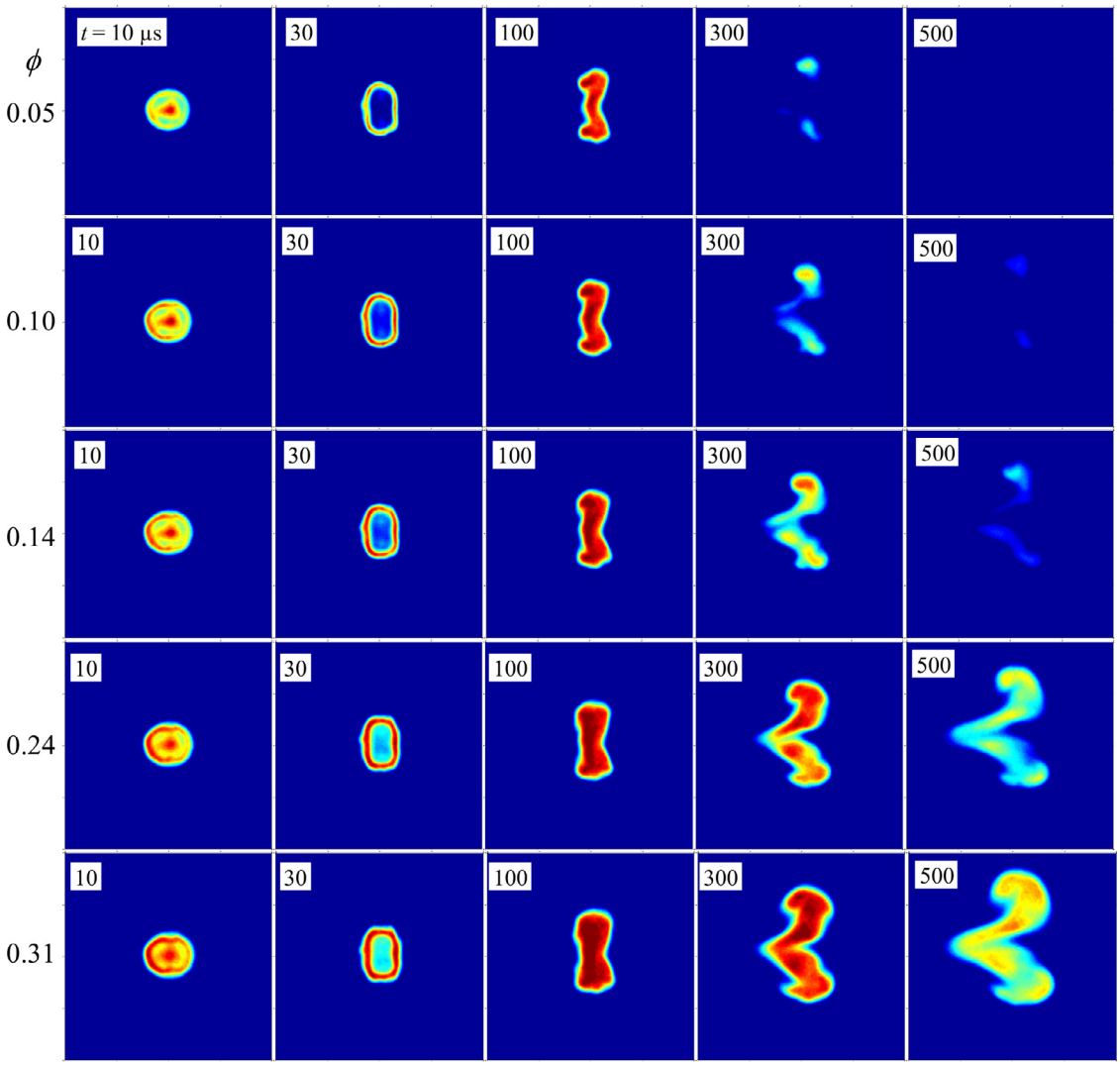

Fig. 11. Mean OH-PLIF images showing the evolution of the flame kernel for H_2/air mixtures of five different equivalence ratios as indicated on the left hand side of each image set. The numbers in the insets are the time delays in μs after the incident laser pulse. All the images are plotted on the same contour scale and contour scheme (rainbow) as of Fig. 3, where red measures maximum and blue indicates minimum intensity. The images are 20 mm × 20 mm in size. The mean pulse energy of the ignition-laser, $E = 126$ mJ.

with H_2 concentration (or ϕ) as shown in Fig. 12(d), similar to that of the CH_4/air presented earlier in Fig. 10(d).

3.6. Effect of flow velocity

The effect of flow velocity V or Reynolds number Re on the flame-kernel development is established by varying the bulk velocity of the $\phi = 0.6$ CH_4/air mixture. The Re is defined at the exit of the burner, based on the burner diameter and the bulk velocity. Experiments are performed at the following three velocities: 90, 470, and 940 cm/s, which translate to the bulk $Re = 575$, 3000 and 6000, respectively. Such a wide range of velocity is chosen to include both laminar and turbulent flow regimes for pipe flow. The OH-PLIF images are acquired at the following time delays: 3, 10, 50, 100, 200, 300, 600, and 1000 μs. The effect of the bulk velocity at a time delay of 600 μs can be observed from the mean OH-PLIF images shown in Fig. 13. In these images, the location of focus of the ignition-laser beam is marked by a white cross for reference. The convective effect of the velocity on the flame-kernel is evident from Fig. 13. Both the large toroids (close to the nozzle and away from it) move by nearly the same distance as a whole unit; however, the front-lobe of the kernel does not. This may be due to the lower velocities away from the nozzle axis. As compared to the flame-kernel at 90 cm/s, the toroids at 470 and 940 cm/s appear to be disintegrated from the respective front-lobes of the flame-kernel. Though the flame-kernel shapes are different, the size of the kernel does not appear to vary significantly.

The effect of higher velocity (or turbulence) can be presented only through the instantaneous realizations. The approximate estimate of the shot-to-shot fluctuation of laser energy is obtained from the H-alpha images. From this estimate, the PLIF images that correspond to minimal energy fluctuations ($< \pm$ 0.5% of the mean energy) of the ignition-laser are selected out of 100 realizations. Figure 14 shows five such sample instantaneous PLIF images at three different velocities. The flame-kernel shapes and sizes are highly repeatable at 90 cm/s. The flame-kernel consists of two segments: upstream and downstream toroids with the respective intact front-lobes. At higher velocities (470 and 940 cm/s), however, three flame-kernel segments are observed: upstream and downstream toroids with a disintegrated front-lobe. This could be due to the increased strain at higher velocities. This hypothesis can be confirmed through simultaneous measurement of the velocity field, which can provide local strain values. This important aspect of strain effects on the flame-kernel will be investigated in future, as it is beyond the scope of the present LIF based study.

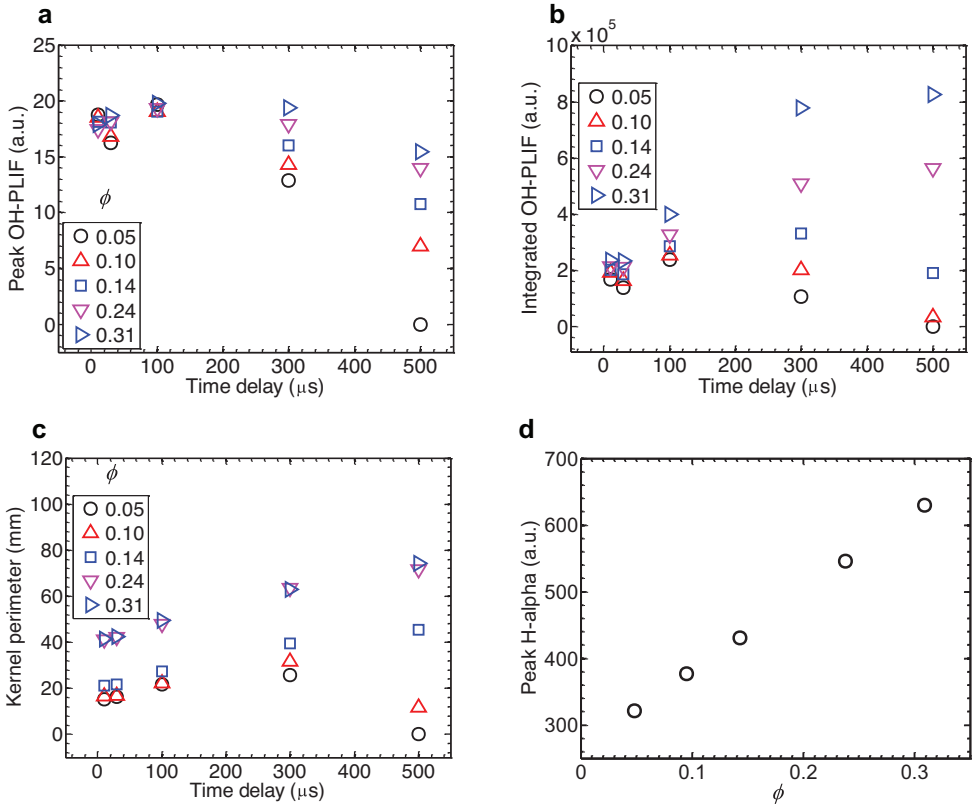

Fig. 12. Effect of equivalence ratio (indicated in legend) for H_2/air mixtures: (a) peak PLIF intensity, (b) spatially-integrated PLIF intensity, (c) flame-kernel perimeter, and (d) H-alpha intensity at 280 ns after the laser pulse. The mean pulse energy of the ignition-laser $E = 126$ mJ.

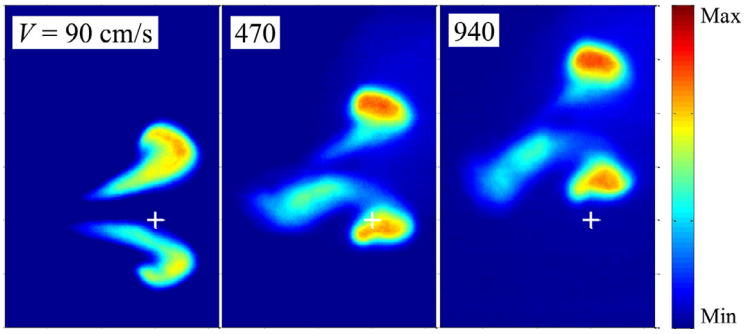

Fig. 13. Mean OH-PLIF images for different velocities at a time delay of 600 μs. The numbers in the insets indicate the bulk velocity V in cm/s. The white cross mark indicates the approximate location of focus of the ignition-laser beam. All the images are plotted on the same contour scale. The images are 30 mm high and 20 mm wide.

The flame-kernel shapes and sizes at 470 and 940 cm/s appear similar, except at 940 cm/s where the size of the front-lobe is shrunk. Another observation from the instantaneous images is the mild increase in the background LIF signal at higher velocities as compared to that at 90 cm/s.

The above qualitative discussion is extended to include the quantitative information from the PLIF images. This information is presented in Fig. 15 along with the H-alpha emission. To demonstrate the validity of the data reduction procedure in the turbulent flow regime, the peak OH-PLIF signal is extracted from the mean OH-PLIF image (Fig. 15(a)) and compared with the mean of the peak OH-PLIF signal obtained from the instantaneous images (Fig. 15(b)), as detailed earlier in Section 3.2. The PLIF data at 3 μs is used only for evaluating the flame-kernel perimeter. The results are qualitatively similar between either of these (Fig. 15(a) or (b)) processing approaches. The OH-LIF signal increases mildly with velocity as shown in Fig. 15(a) and (b). The LIF signals are nearly identical at $V = 470$ and 940 cm/s. The spatially integrated LIF intensities (Fig. 15(c)) at these two velocities are also nearly identical. The integrated signals at these velocities measure significantly higher than at 90 cm/s during 100–300 μs. However, at 600 μs, the integrated signal is almost identical for all the three velocities. A similar observation is noted for the flame-kernel perimeter evolution shown in Fig. 15(d). The flame-kernel perimeters are nearly identical at $V = 470$ and 940 cm/s. During the timescale of 0–100 μs, turbulence does not appear to affect the kernel growth. However, during 100–300 μs, the flame-kernel size is enhanced, probably due to the turbulence (at $V = 470$ and 940 cm/s), but during 300–600 μs, the growth rate reduces to that of 90 cm/s. The plots shown in Fig. 15(c) and (d) do not include data points corresponding to 940 cm/s at 1000 μs. At this velocity and time delay, a part of the flame-kernel gets convected outside the field-of-view.

The increase in the velocity influences the two competing effects that contribute towards the development of flame-kernel: first, the increase in the strain rate, and second, the increase in the

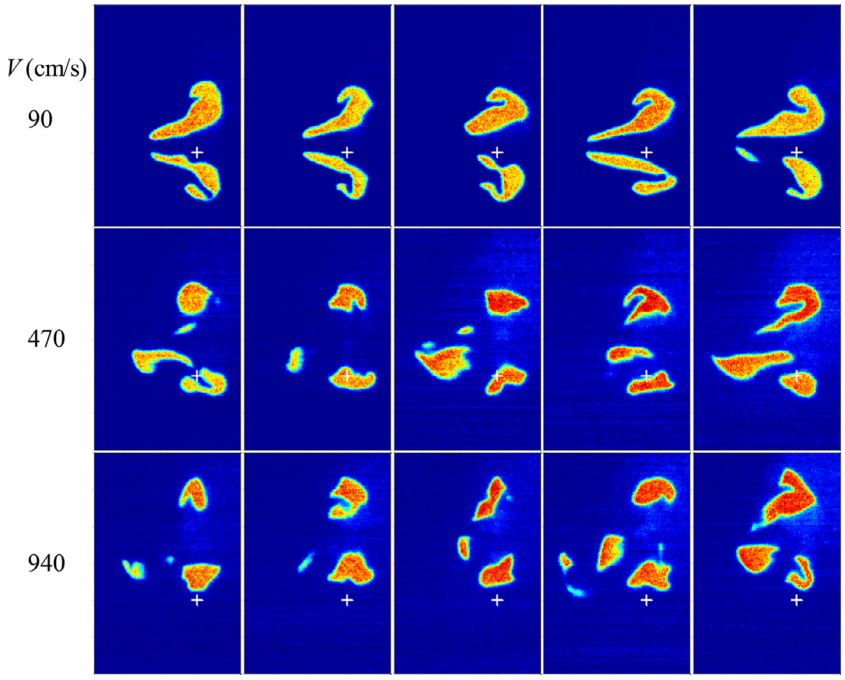

Fig. 14. Instantaneous OH-PLIF images at a time delay of 600 μs at different bulk velocities *V* (indicated on the left hand side in cm/s). The white cross mark indicates the approximate location of focus of the ignition-laser beam. All the images are plotted on the same contour scale, similar to the contour scheme (rainbow) of Fig. 12, where red indicates maximum and blue minimum. The images are 30 mm high and 20 mm wide.

flame-kernel surface area. At lower velocities, the flame-kernel could grow without getting fragmented, which is permitted by a low strain rate. The strain rate increases with velocity, which causes local extinction of the flame-kernel, as discussed earlier in the context of Fig. 14. Simultaneously, the increased velocity is expected to increase the turbulence level, which in turn wrinkles the flame-kernel fronts, thus increasing the surface area, which consequently enhances the flame-kernel spread. These two competing effects may balance each other. Hence, the flame-kernel perimeter in the turbulent flow regime is not significantly higher than that of the laminar flow regime, and it measures identical at the velocities of 470 and 940 cm/s. The H-alpha signal decreases exponentially with velocity as shown in Fig. 15(e). This is probably due to the reduced residence time associated with increase in the flow velocity.

4. Conclusions

The development of the flame-kernel in laser-induced spark ignited mixtures is investigated in detail for the first time using the OH-PLIF technique and H-alpha emission from the spark. The laser-induced spark is characterized first in pure air. The temporal profile of the H-alpha emission suggests that the plasma time-scales are well below 1 μs. The H-alpha intensity variation is found to be linear with the incident laser energy.

The temporally and spatially resolved OH-PLIF images show the detailed sequence of the flame-kernel formation. A large counter-rotating trailing edge toroid appears around 50 μs, while a small leading edge toroid becomes apparent around 100 μs. The larger toroid grows and prevails till 1000 μs, while the smaller toroid disappears with the inception of a front-lobe around 200 μs. The shape of these flame-kernels is in accordance with the studies reported in the past. The variation of the flame-kernel perimeter with time exhibits distinct slopes over different time-scales. The growth of the kernel perimeter saturates around 700 μs. The OH-LIF intensity varies systematically with time. The LIF signal peaks around 200 μs and then drops at a constant rate till 1000 μs.

The flame-kernel size increases with the laser energy. This increase in the kernel size is attributed to stronger shock-waves. The growth of the flame-kernel perimeter indicates distinct positive and negative peaks associated with shock- and expansion- waves respectively. The higher laser energy does not lead to efficient kernel growth, in general.

The effect of three gas compositions, namely, CH_4/air, CH_4/CO_2/air, and CH_4/H_2/air is investigated at a given adiabatic flame temperature. The evolution of the LIF signal is nearly identical for all the three mixtures, with a distinct local peak around ∼200 μs. However, the spatially-integrated LIF signal and the kernel perimeter measure significantly higher for the CH_4/H_2/air relative to the other two mixtures. The trends in the evolution of the integrated LIF and flame-kernel perimeter till ∼100 μs are identical across the mixtures: initially (<100 μs), the kernel perimeter for the CH_4/CO_2/air follows that of the CH_4/H_2/air and subsequently (> 100 μs), shifts to that of the CH_4/air. The early flame-kernel evolution in the ignition process is concluded to be independent of gas compositions, at least till 100 μs. The H-alpha values for these three gas compositions are commensurate with the respective H-atom fraction.

The flame-kernel development around the LFL is also investigated as a function of fuel concentration for the CH_4/air mixture. The OH-LIF signal is less sensitive to fuel concentration during 10–200 μs. Thereafter, the LIF signal is distinctly low for the mixture below LFL. The flame-kernel perimeter increases for the first 200 μs, and thereafter, the trend changes depending on the fuel concentration. For mixtures below the LFL, the perimeter begins to drop during 200–300 μs. For a mixture just above the LFL, the perimeter growth saturates during 300–600 μs and then drops. On the other hand, for mixtures well above the LFL, the perimeter consistently grows till 1000 μs, however at a lower growth rate. The variation of the H-alpha signal with the fuel concentration is nearly linear. Very similar trends are noted in the H_2/air mixtures as well.

The effect of velocity on the flame-kernel evolution is studied. The flow velocities correspond to laminar, transition, and turbulent regimes, with $Re = 575$, 3000, and 6000, respectively. At higher velocities, the front-lobe gets disintegrated from the respective toroidals, and thus the flame-kernel appears in three different segments. The size of the front-lobe shrinks with increase in the velocity. The local extinction of the flame-kernel may be due to higher strain attributed

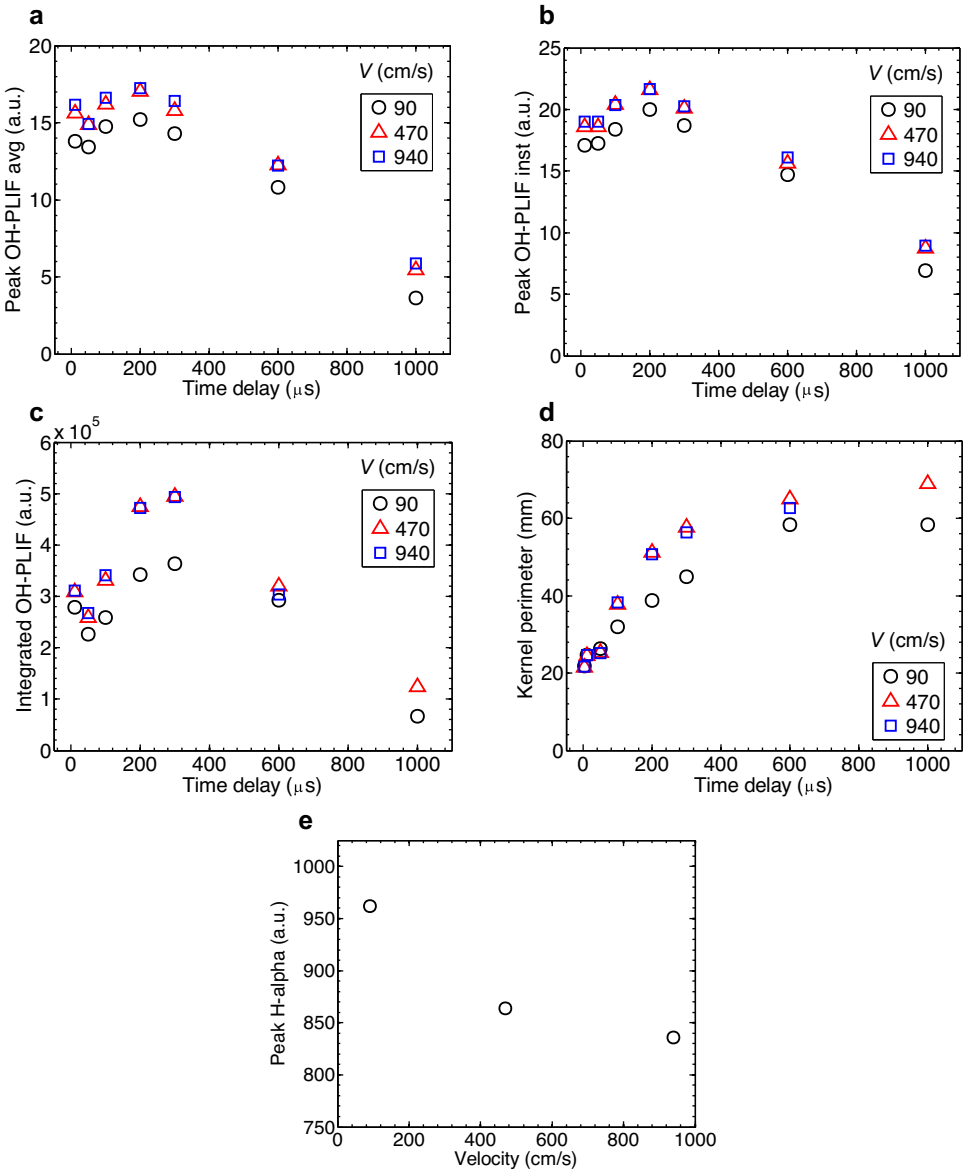

Fig. 15. Effect of velocity on flame kernel development in $\phi = 0.60$ CH_4/air mixture: (a) peak PLIF intensity extracted from the mean images; (b) mean of the peak LIF intensity extracted from the instantaneous images; (c) spatially-integrated PLIF intensity; (d) flame-kernel perimeter, all at different flow velocities indicated in the legends, in cm/s; and (e) H-alpha emission at 280 ns after the laser pulse. The mean pulse energy of the ignition-laser $E = 187$ mJ.

to higher velocities. The OH-LIF signal is less sensitive to the velocity. The flame-kernel perimeter is identical for the first 50 μs. From 100–300 μs, the perimeter measures mildly higher for $Re = 3000$ and 6000. At these two Re, the perimeters are nearly identical. This could be explained as the balance between the following two competing effects. The increase in the velocity is associated with, first: an increase in the strain rate that causes local extinction and thus decreases the flame-kernel growth, and second: an increase in the turbulence levels that facilitates increased flame-kernel surface area through wrinkling, which increases the flame-kernel growth. Consequently, the kernel perimeter is weakly dependent on the flow velocity. The H-alpha signal decreases asymptotically with the flow velocity, most likely due to the reduction in the residence time of the mixture at higher velocities.

Acknowledgments

The authors acknowledge EPSRC and UKIERI for support through grants EP/G063788/1 and UKUTP201100363 respectively. The authors thank Prof. E. Mastorakos (University of Cambridge, UK) for helpful discussions and suggestions.

References

[1] P.D. Ronney, Laser versus conventional ignition of flames, Opt. Eng. 33 (1994) 510–521.
[2] E. Mastorakos, Ignition of turbulent non-premixed flames, Prog. Energy Combust. Sci. 35 (2009) 57–97.
[3] S.A. Ramsden, P. Savic, A radiative detonation model for the development of a laser-induced spark in air, Nature 64 (1964) 1217–1219.
[4] N.M. Witriol, B.E. Forch, A.W. Miziolek, Modeling laser ignition of combustible gases, 27th JANNAF Combustion Meeting, The Chemical Propulsion Information Agency, (1990).
[5] E. Yablonovich, Self-phase modulation and short pulse generation from laser breakdown plasmas, Phys. Rev. A 10 (1975) 1888–1895.
[6] L.J. Radziemski, D.A. Cremers (Eds.), Laser-Induced plasmas and applications, Dekker, New York, 1989.
[7] T.X. Phuoc, Laser-induced spark ignition fundamental and applications, Opt. Lasers Eng. 44 (2006) 351–397.
[8] J.A. Syage, E.W. Fournier, R. Rianda, R.B. Cohen, Dynamics of flame propagation using laser induced spark initiation: ignition energy measurements, J. Appl. Phys. 64 (1988) 1499–1507.

[9] H. Kopecek, H. Maier, G. Reider, F. Winter, E. Wintner, Laser ignition of methane–air mixtures at high pressures, Exp. Therm. Fluid Sci. 27 (2003) 499–503.
[10] J.L. Beduneau, Y. Ikeda, Application of laser ignition on laminar flame front investigation, Exp. Fluids 36 (2004) 108–113.
[11] M. Weinrotter, H. Kopecek, M. Tesch, E. Wintner, M. Lackner, F. Winter, Application of laser ignition to hydrogen–air mixtures at high pressures, Int. J. Hydrog. Energy 30 (2005) 319–326.
[12] M. Weinrotter, H. Kopecek, M. Tesch, E. Wintner, M. Lackner, F. Winter, Laser ignition of ultra-lean methane/hydrogen/air mixtures at high temperature and pressure, Exp. Therm. Fluid Sci. 29 (2005) 569–577.
[13] R. Hickling, W.R. Smith, Combustion bomb tests of laser ignition, SAE Tech., paper 740114 (1974).
[14] P.B. Dickinson, A.T. Shenton, J.D. Mullett, G. Dearden, A. Scarisbrick, Prospects for laser ignition in gasoline engine control, 10th International Symposium on Advanced Vehicle Control (AVEC10), 2010, pp. 22–26.
[15] C. Grey Morgan, Laser-induced breakdown of gases, Rep. Prog. Phys. 38 (1975) 621–665.
[16] M. Tsunekane, T. Inohara, A. Ando, N. Kido, K. Kanehara, T. Taira, High peak power, passively Q-switched microlaser for ignition of engines, IEEE J. Quantum Electron. 46 (2010) 277–284.
[17] H. Kopecek, S. Chareareh, M. Lackner, C. Forsich, F. Winter, J. Klausner, G. Herdin, M. Weinrotter, E. Wintner, Laser ignition of methane-air mixtures at high pressures and diagnostics, J. Eng. Gas Turbines Power 127 (2005) 213–219.
[18] J.D. Dale, P.R. Smy, R.M. Clements, Laser ignited internal combustion engine - An experimental study, SAE Technical, paper 780329 (1978).
[19] D. Bradley, C.G.W. Sheppard, I.M. Suardjaja, R. Woolley, Fundamentals of high-energy spark ignition with lasers, Combust. Flame 138 (2004) 55–77.
[20] F.J. Weinberg, J.R. Wilson, A preliminary investigation of the use of focused laser beams for minimum ignition energy studies, Proc. R. Soc. Lond. A 321 (1971) 41–52.
[21] J. Beduneau, B. Kim, L. Zimmer, Y. Ikeda, Measurements of minimum ignition energy in premixed laminar methane/air flow by using laser induced spark, Combust. Flame 132 (2003) 653–665.
[22] T. Lee, V. Jain, S. Kozola, Measurements of minimum ignition energy by using laser sparks for hydrocarbon fuels in air: propane, dodecane, and Jet-A fuel, Combust. Flame 125 (2001) 1320–1328.
[23] T.X. Phuoc, F.P. White, Laser-induced spark ignition of CH/air mixtures, Combust. Flame 119 (1999) 203–216.
[24] T.A. Spiglanin, A. Mcilroy, E.W. Fournier, R.B. Cohen, J.A. Syage, Time-resolved imaging of flame kernels: laser spark ignition of H_2/O_2 /Ar mixtures, Combust. Flame 102 (1995) 310–328.
[25] S. Brieschenk, S. O'Byrne, H. Kleine, Laser-induced plasma ignition studies in a model scramjet engine, Combust. Flame 160 (2013) 145–148.
[26] Y. Chen, J.W.L. Lewis, Visualization of laser-induced breakdown and ignition, Opt. Expr. 9 (2001) 360–372.
[27] M. Lackner, S. Chareareh, F. Winter, K.F. Iskra, D. Rüdisser, T. Neger, H. Kopecek, E. Wintner, Investigation of the early stages in laser-induced ignition by Schlieren photography and laser induced fluorescence spectroscopy, Opt. Expr. 12 (2004) 4546–4557.
[28] C. Cardin, B. Renou, G. Cabot, A.M. Boukhalfa, Experimental analysis of laser-induced spark ignition of lean turbulent premixed flames: New insight into ignition transition, Combust. Flame 160 (2013) 1414–1427.
[29] D.K. Srivastava, K. Dharamshi, A.K. Agarwal, Flame kernel characterization of laser ignition of natural gas–air mixture in a constant volume combustion chamber, Opt. Laser Eng. 49 (2011) 1201–1209.
[30] C.F. Kaminski, J. Hult, M. Aldén, S. Lindenmaier, A. Dreizler, U. Maas, M. Baum, Spark ignition of turbulent methane/air mixtures revealed by time-resolved planar laser-induced fluorescence and direct numerical simulations, Proc. Combust. Inst. 28 (2000) 399–405.
[31] D.A. Santavicca, C. Ho, B.J. Reilly, T.W. Lee, Laser induced spark ignition of methane–oxygen mixtures, Report No. NASA-CR-188689, Pennsylvania State University, University Park, PA, USA, 1991.
[32] M.H. Morsy, Y.S. Ko, S.H. Chung, Laser-induced ignition using a conical cavity in CH-Air mixtures, Combust. Flame 119 (1999) 473–482.
[33] G. Dearden, T. Shenton, Laser ignited engines: progress, challenges and prospects, Opt. Expr. 21 (2013) A1113–A1125.
[34] W. Qin, Y-L. Chen, J.W.L. Lewis, Time-resolved temperature images of laser-ignition using OH two-line laser-induced fluorescence (LIF) thermometry, IFRF Combust. J., Tech. Rep. Article Number 200508 (2005).
[35] M. Kono, K. Niu, T. Tsukamoto, Y. Ujiie, Mechanisms of flame kernel formation produced by short duration spark, Symp. (Int.) Combust. 22 (1989) 1643–1653.
[36] M.H. Morsey, S.H. Chung, Numerical simulation of front-lobe formation in laser-induced spark ignition of CH/air mixtures, Proc. Combust Inst. 29 (2002) 1613–1619.
[37] S.A. Ramsden, W.E.R. Davies, Radiation scattered from the plasma produced by a focused ruby laser beam, Phys. Rev. Lett. 13 (1964) 227–229.
[38] R.J. Kee, J.F. Grcar, M. Smooke, J.A. Miller, PREMIX: A FORTRAN program for modeling steady one-dimensional flames, Report No. SAND85-8240, Sandia National Laboratories, Livermore, CA, USA, 1985.
[39] K.L. Cashdollar, I.A. Zlochower, G.M. Green, R.A. Thomas, M. Hertzberg, Flammability of methane, propane, and hydrogen gases, J. Loss Prev. Proc. 13 (2000) 327–340.